An edited version of this paper was published by AGU.

Radar scattering of the ocean surface and sea-roughness properties: A combined analysis from dual-polarizations airborne radar observations and models in C band

Alexis Mouche,1,2 Danièle Hauser,3 and Vladimir Kudryavtsev,4

1IFREMER, Plouzané, France.
2Formerly at CETP-IPSL/CNRS/UVSQ, Vélizy, France.
3CETP-IPSL/CNRS/UVSQ, Ve´lizy, France.
4NIERSC, St Petersburg, Russia.

Abstract: An analysis of radar observations in C band combined with models is proposed to study some of the ocean surface properties and their relation with the sea surface backscatter. The electromagnetic part of the models is of different kinds: composite Bragg model with or without including effect of wave breaking zones on the normalized radar cross-section (NRCS), geometrical optics approximation and small-slope approximation model. The surface description is based on the wave spectrum proposed by Kudryavtsev et al. (2003), but tests with the spectrum of Elfouhaily et al. (1997) are also discussed to assess our conclusions. The originality is to use not only the NRCS in HH and VV polarizations, but also their difference in linear units. First, we show that the upwind-to-downwind anisotropy of the radar signal cannot be explained entirely by the modulation of Bragg waves by longer surface waves, but that an additional nonpolarized contribution must be invoked to explain it, consistently with scattering from zones of enhanced roughness associated with breaking waves. Then, combining a composite model and observations in the two polarizations, we assess the contribution of the nonpolarized backscatter on the total NRCS. Finally, the proposed full model, which takes into account the nonpolarized contribution over breaking zones, gives good agreement with the observed polarization ratio and with the NRCS in each polarization.

Keywords: radar cross-section; sea surface anisotropy; wave breaking.

Introduction

The capabilities of new sensors like the ASAR on board ENVISAT or the forthcoming RADARSAT-2 gives the capabilities of measuring the normalized radar cross-section (NRCS hereinafter) from the same area in HH and VV polarization (NRCS-HH and NRCS-VV hereinafter respectively for the NRCS in HH and VV polarization) for a wide range of incidence angles in C-Band. However, the interest of combining the two co-linear HH and VV polarizations over the ocean to retrieve geophysical parameters like wind, wave or currents has not been fully investigated yet. Furthermore, due to the importance of past missions (ERS in particular) a lot of studies, both empirical and theoretical, have been mainly devoted to the VV-polarization and the transposition of results to the HH polarization is still a matter of debate.

In particular, a lot of models based on a theoretical ground reproduce quite well the main trends of the VV backscatter as a function of incidence or wind speed, but fail to predict the NRCS in HH polarization at intermediate and large incidence angles. This is the case for the standard or advanced composite models (e.g. [*Valenzuela*, 1978, *Plant*, 1986; *Romeiser et al.*, 1997]), which combine a description of the Bragg scattering mechanism with local tilting effects due to longer underlying waves. Based on wind-wave tank measurements, [*Plant et al.*, 1999] try to explain this shortcoming by taking into account additional effects due to bound short waves linked to the longer waves, which modify the Bragg scattering. However, in the same publication, arguing that bound, tilted waves on the ocean have a too small spectral density in comparisons to the freely propagating wind-generated waves, *Plant et al.* [1999] conclude that bound waves effect is not sufficient to fully explain the level of the NRCS-HH in the open ocean. *Plant* [2003] proposes to consider non-Bragg scattering through sea spray close to the surface in addition to the bound, tilted waves to obtain an agreement with the HH polarized observations. *Kudryavtsev et al.* [2003], based on the works done by *Ericson et al.* [1999] and *Phillips* [1988], propose to take into account zones of enhanced roughness associated with the wave breaking process, to explain the observed polarization ratio (ratio of VV over HH backscatter). They suggested that enhanced surface roughness associated with an individual breaker contributes to the NRCS by means of the specular reflection in agreement with the work of *Ericson et al.* [1999]. The originality of this approach is a consistent description of the wave height spectrum and the wave breaking properties needed for the NRCS model.

In the above-mentioned composite radar scattering models, the main drawback is the need to specify a dividing parameter, which separates the scales of the long tilting waves from the scale of the shorter Bragg waves. For that reason, and in order to merge the two asymptotical electromagnetic theories of Kirchhoff and Small Perturbation (or Bragg regime) regimes, "unified" models have been developed. Among these, the small slope approximation model of *Voronovich* [1994] has been tested for ocean surface conditions. However, in *Voronovich and Zavorotny* [2001] it is clearly shown that this model does not overcome the problem encountered with the two-scale model: even if NRCS-VV can be well-reproduced as a function of incidence, the model also fails in HH polarization, in its 1st (SSA-1) and 2nd (SSA-2) order approximations. To overcome the differences between data and model in HH polarization, *Voronovich and Zavorotny* [2001] propose also to take into account the steep waves at the sea surface due to wave breaking. They consider that the breaking waves cannot be considered in the frame of the small slope approximation due to their too steep slopes. Thus, they introduce a contribution to the NRCS from specular reflection depending on the density probability of the occurrence of steep slopes to explain the NRCS-HH. This density is determined fully empirically, to adjust their model on Ku-Band data and leads to satisfying results.

Another major issue these recent years is to better understand and describe the behavior of

the NRCS versus azimuth with respect to the wind direction. For the upwind to downwind asymmetry, the standard approach is to introduce a hydrodynamic modulation of short waves by long waves due to straining effects and eventually to aerodynamics effects over the long wave profile (see e.g. [*Plant,* 1986; *Romeiser et al.,* 1997; *Kudryavtsev et al.* 2003]) . The shortcoming of this approach is the need for an assumption on the relaxation time of the short waves [*Romeiser et al.,* 1997]. Also, to model the upwind-to-downwind asymmetry *Kudryavtsev et al.* [2003] proposed to account for the perturbation of the surface due to wave breaking effects. In particular, in Ka-band this asymmetry is associated with trains of parasitic capillaries (which are spread on the leeward slope of the small scale breaking waves), and in other radar bands the upwind-to-downwind asymmetry can be associated with azimuth anisotropy of breaking zones. Concerning the upwind to crosswind asymmetries of the radar signal, most of the studies show that the main governing parameter is the angular description of the sea surface spectrum. *McDaniel* [2001] and *Voronovich et al.* [1995] show how sensitive are the upwind-to-crosswind ratio of a radar backscatter prediction with a small-slope approximation model. They came to the conclusion that the frequently used models of *Elfouhaily et al.* [1997] or *Banner* [1990] for the angular distribution of the wave height spectrum have to be re-examined to obtain agreement between model and observations of the up/crosswind backscatter asymmetry. Results shown by *Kudryavtsev et al.* [2003] obtained with a different electromagnetic model and a different angular dependence of the wave spectrum also show – see their figure 15b-, that the upwind to crosswind asymmetry still suffers from a disagreement between observations and model.

In this context, we propose here a study on the different (Bragg and non Bragg) contributions to the NRCS and on the angular behavior of the radar backscatter in relation with the surface properties. This study is based on C-Band radar observations, collected by our group with the airborne radar called STORM [*Hauser et al.,* 2003] during the VALPARESO experiment (see [*Mouche et al.,* 2005] and section 2). The originality is that our study is based on combinations of HH and VV radar cross-sections over a large range of incidence angles, and azimuth angles, in a variety of wind and wave conditions. These observations, compared to results from simplified versions of a two-scale model are used to identify the various mechanisms that can impact on the azimuth behavior of the radar backscatter, and to separate the different contributions to the total NRCS. The sea surface description used as input to the electromagnetic model is almost similar to the one presented in *Kudryavtsev et al.* [2003] (see annex 1). We choose this physical spectrum because of its consistency in the description of the wave height spectrum and the breaking wave statistics. For some comparisons, we use also the wave spectrum model of *Elfouhaily et al.* [1997].

Section 2 gives an overview of the experimental data set. Section 3 gives a summary on the electromagnetic models and surface description used in the study. Section 4 discusses the general features of the NRCS in VV and HH polarizations inferred from our data, and presents comparisons with the two-scale and the SSA models (developed at the first order). Section 5 deals with the analysis of the data in a dual polarization mode to assess the two-scale model and infer properties of the sea surface anisotropy, and of the non-polarized part of the backscatter. Section 6 presents a comparison of our observations with the results of the so-called "full" model, that is a slightly revised version of the model proposed by *Kudryavtsev et al.* [2003] which include a non-polarized part in addition to a two scale Bragg model. The comparisons are presented for the NRCS in VV and HH polarization as well as for the polarization ratio, as a function of incidence, azimuth angle and wind speed. Section 7 recalls the main results of the paper and concludes our study.

1. Experiment overview

The VALPARESO experiment was carried out by CETP, in collaboration with IFREMER and Météo-France, in the context of the ASAR (Advanced Synthetic Aperture Radar) geophysical calibration and validation exercise performed and supported by ESA after the launch of ENVISAT. It took place from 19 October to 21 November 2002 off the coasts of France and UK (near-Atlantic coasts of France and English Channel).

The main component of this experiment was the airborne radar called STORM. In the experimental zone, the meteo-oceanic buoy "PHAROS" (48°31'42"N, 5°49'03"W) was frequently over-flown by STORM. This buoy provided measurements of wind and ocean wave spectra for the whole duration of the campaign with a 1-hour sampling frequency.

The characteristics of STORM and details on the data processing have been described elsewhere in details [*Hauser et al.*, 2003; *Mouche et al.*, 2005]. We recall here only the main features.

STORM uses an FM/CW (Frequency Modulated Continuous Wave) transmitted waveform, transmitted every 8 ms alternatively in H and V polarization. It receives simultaneously in both H and V channels. Isolation between polarizations is better than 30 dB for the transmitting antenna, and 40 dB for the receiving antenna.

Two modes of operation were used to cover a large range of incidence. In the first one, the plane flew along horizontal straight lines flights and the antenna scanned over 360° in azimuth; in this configuration the range of incidence angles is about 10 to 35°. In the second mode, the plane performed circle flights with a 15° roll and the antenna was fixed on one side so as the mean incidence angle was about 35°, and the range of incidences than can be analyzed is about 20 to 45°. This latter mode in circle patterns was used exclusively in the vicinity of the PHAROS buoy location.

After post-processing the data set as used here, consists in:
- VV and HH NRCS for incidence angles from 10 to 35° averaged in 1° incidence bins and every 2.3° in azimuth for the first acquisition mode (straight line patterns)
- VV and HH NRCS for incidence angles from 20 to about 45° averaged in 1° incidence bins, and every 1.2° in azimuth for the second acquisition mode (circle flight patterns).

Each individual value of NRCS used in this study is representative of an illuminated area of about a few tens of meters in the elevation direction by 300 to 400 m in the azimuth direction (depending of the mode of operation and incidence angle). Upwind, downwind, crosswind values of the NRCS have been estimated from fits of Fourier series on data sets acquired over 1.5 to 3 minutes (3 azimuth scans of 360°), representative of surface areas of about 4 km x 10 km for the linear mode of flight, and about 5 km x 5 km for the circle flight mode.

Note that we have not used the HV observations in the present study, mainly because the signal-to noise ratio in this configuration is rather low at incidence angles above 20-25° : the measured radar HV cross-section is about -25 dB smaller than the VV NRSC at the incidence of 20°.

In order to relate our NRCS data to the sea surface conditions, we limit our analysis of the STORM data to files acquired close to the PHAROS buoy (±0.2° in latitude and longitude from the buoy position). The meteorological conditions of our data set cover a large range of wind speed (from 4 to 16 m s^{-1}).

2. Surface description and modeling of the normalized radar cross-section

In the following most of the results and discussions are based on the elements of the electromagnetic model proposed by *Kudryavtsev et al.* [2003] (KHCC hereafter) with only slight modifications presented in appendix. It is sufficient to recall here that the model of

KHCC for the NRCS is expressed as the sum of 3 terms: a composite Bragg term (two-scale or TS model), a geometrical optic (GO) term to account for quasi-specular reflection at small incidence, and a third term due to scattering from surface areas affected by wave breaking which is similar for both polarizations (HH and VV). This latter part is called the non-polarized part and not accounted for in the first part of the discussion (up to section 5.2). In the following, we will refer to the sum of the first two terms as the TS+GO model. When the first term only is implied, we will refer to it as the TSM (two-scale model)

To assess our conclusions, we also present in section 4.1, the model of *Voronovich* [1994] based on the "Small Slope Approximation" in its first order version. This model is based on the expansion of the scattering amplitude in terms of the roughness slope. Its main advantages compared to the TS+GO model are: (i) it does not require a partitioning of the surface in two scales; (ii) it is more appropriate to describe the NRCS over a large range of incidence angles typically from 0 to 60°.

To run these models, a description of the sea surface is required. This description consists in a directional wave height (or directional wave curvature spectrum). This wave height spectrum is decomposed in a low frequency part (for the dominant waves around the peak wave number k_p, up to about 10 k_p), and a high-frequency part with wavenumbers larger than 10 k_p (equilibrium range of the spectrum). We use in the following, the wave curvature spectrum proposed by KHCC (with slight modifications as indicated in appendix). It is the weighted sum of the low-frequency part chosen as the classical empirical model proposed by *Donelan et al.* [1985] and of an equilibrium part that is solution of the wave action balance equation (see appendix). The directional spreading of the equilibrium part of the wave spectrum is not fixed explicitly but is the result of the solution of the wave action balance equation. Hence, the KHCC model for the surface is derived from the wave energy balance equations possessing 3 tuning constants that are chosen so as to fit the spectrum model to observations (see KHCC for more details). To calculate the non-polarized part of the NRCS, the model is based on the statistic of wave breaking fronts, which is expressed as a function of the wave spectrum (see appendix).

In order to assess our conclusions, we carried out some comparisons by using the same electromagnetic model but run with another surface model, namely the "unified wave spectrum" proposed by *Elfouhaily et al.* [1997]- hereafter ECKV97. In this case, the analytical expression of the wave curvature spectrum was chosen by ECKV97 to be in agreement with various experimental works and to provide a continuous formulation for the low-frequency and high frequency parts of the spectrum. The directional spreading of the wave spectrum in this model is imposed empirically without invoking any physical mechanisms that occur on the sea surface.

3.   General features of the NRCS in VV and HH polarizations

In this section, we show a complete presentation of the NRCS in both polarizations as a function of incidence angle, wind speed and azimuth angle obtained from our radar STORM. When this is relevant, the STORM data are compared below to the empirical functions of two CMOD models, namely the CMOD5 model (*Hersbach et al.*, 2005) and the CMOD2-I3 model (*Bentamy et al.*, 1994). Both were established to retrieve the wind vector from C-Band scatterometers (ERS1-ERS2). We choose these two, because CMOD5 is the most updated one, and CMOD2-I3 was established by using in situ observations. In this section 4, and in Figures 1 to 7, these experimental results are compared to the TS+GO model (and to the SSA-1 model in Fig.1). Note that the main modifications of the TS part compared to its original version presented in KHCC (see appendix for details) is that we ignore hydrodynamics effects to model upwind-to-downwind asymmetry. The same figures (Fig1 to 7) will be discussed

again in section 6, for comparisons with the full model (solid lines in the following figures).

3.1.   NRCS in VV- and HH-polarizations as a function of incidence and wind speed.

Figure 1 presents the NRCS versus incidence angle in the upwind direction, for all the cases of observations in conditions of a 10 m s^{-1} wind speed, for the VV (Fig. 1a) and HH (Fig.1b) polarizations. STORM observations are shown as black full circles, whereas the TS+GO model is the dashed line, and the SSA-1 model corresponds to the dashed-dotted lines with star symbols.

From the observations, we observe the well-known decreasing trend of the NRCS with increasing incidence angle. We note also the difference between HH and VV polarization for incidence angles greater than 30° where the decrease of NRCS-HH with incidence angle is more steep than for NRCS-VV. The NRCS predicted by the TS+GO model run with the KHCC wave spectrum (dashed lines) is in good agreement with the STORM data in VV (Fig.1a). In opposite, it fails (underestimation) in HH polarization for incidence angles greater than 30° (dashed line in Fig.1b). The same conclusion holds with the SSA-1 model (dashed-dotted line with stars). In this case, the underestimation in HH with respect to the data is even larger. *Voronovich and Zavorotny* [2001] also showed that when extending their approximation to the second order (SSA-2), the model still underestimates the observed NRCS. Note that considering azimuthally averaged data leads to exactly the same conclusion (not shown). Thus, in conditions where models TS+GO, SSA-1 or SSA-2 are in agreement with VV observations, they underestimate the NRCS-HH at incidence angles larger than 30°. Since we get quite similar conclusions for the SSA-1 model compared to the TS+GO model, we will not further consider the SSA-1 model in the discussions below.

The different trend of the HH and VV NRCS with incidence leads to a polarization ratio that is also dependent of the incidence. *Mouche et al*. [2005] showed that the polarization ratio (defined as the ratio of VV- over HH- NRCS in linear units) increases rapidly with incidence for angles larger than 30°. They also showed that a standard composite Bragg model is not able to reproduce this trend.

Figure 2 shows the NRCS versus wind speed at the incidence angle of 37.5° (±0.5°), in VV- (Fig. 2a) and HH- (Fig. 2b) polarizations. STORM data are again shown as black full circles. We observe an increasing trend of the NRCS with wind speed for both polarizations. The agreement between our STORM data set in VV and the two CMOD-models (dashed-dotted line with circle symbols for CMOD5, dashed-dotted line with stars symbols for CMOD2-I3) is very good. The TS+GO model run with the KHCC surface spectrum (dashed lines) underestimates the experimental values of NRCS slightly in VV and more significantly in HH polarization over the whole range of wind speeds considered in this study. Nevertheless, the sensitivity of the TS+GO model to wind speed is in rather good agreement with the observations.

3.2.   Azimuth behavior of the NRCS in HH and VV polarizations

Figure 3 presents the NRCS versus azimuth angle at 40.5° (±0.5°) incidence angle and a 14 m s^{-1} wind speed, in VV- (Fig 3a) and HH- (Fig 3b) polarizations. The vertical bar indicates the downwind direction measured at the PHAROS buoy during the data acquisition. There is a clear bi-harmonic behavior of the experimental NRCS in both polarizations with upwind-to-downwind (UD) and upwind-to-crosswind (UC) asymmetries. The first maximum is in the upwind direction while the second is in the downwind direction and the two minima are in the crosswind directions. The UD asymmetry of the data is higher for the HH polarization. In

opposite, the UC asymmetry is larger in VV. These differences between VV- and HH-polarizations in the UD and UC asymmetries lead to an azimuth dependence of the polarization ratio, as shown in *Mouche et al.* [2005]. Indeed the polarization ratio shows a maximum in the downwind direction (see also comments on Fig16c in section 6), which exceeds the second maximum of the upwind direction by about 1 dB at the incidence angle of 40°. In the crosswind direction the PR is about 1.5 dB smaller than its value in the downwind direction for a 40° incidence angle. These results led *Mouche et al.* [2005] to propose an empirical polarization ratio model, which accounts for these variations with azimuth.

The TS+GO model (dashed lines) reproduces an harmonic behavior in HH and VV polarizations of the observations, but with a mean underestimate in the case of HH, as expected from Figure 1. In both VV and HH polarizations, note however that the UD asymmetry is not reproduced. This is quite normal since no hydrodynamic effect has been introduced in the model part. The UC asymmetry is rather well reproduced by the TS+GO model in the conditions of this plot (high wind, large incidence).

Figure 4 presents the UD asymmetry versus incidence angle for a 10 m s^{-1} wind speed (± 1 m s^{-1}) in both polarizations. The observed UD ratio in HH polarization clearly increases with incidence angle for incidence angles larger than 30° (Fig.4b), reaching 2.0 dB at 40°. The trend is not so obvious in VV polarization (Fig.4a). But the mean value of the UD ratio reaches about 0.5 dB at 40°, in consistency with the CMOD2-I3 and CMOD5 models (dashed-dotted lines with star and circles, respectively) which give an UD ratio of 0.5 and 0.8 dB, respectively at this incidence. These two empirical models also confirm the increasing trend of the UD ratio with incidence angle. As already mentioned, the theoretical approach which consists in combining the TS+GO model with a wave spectrum without taking into account hydrodynamic effects is not able to reproduce the upwind to downwind asymmetry (dashed line). When the hydrodynamic effect is taken into account as proposed in *Kudryavtsev et al.* [2003] - dotted lines in Fig. 4a-b-, the agreement with the data is much better for VV but not for HH. In this latter case, the TS+GO model still clearly underestimates the UD asymmetry for incidence angle larger than 30°. This suggests that other phenomena may play a role in the UD asymmetry. The same conclusion can be extracted from the results of *Romeiser et al.* [1997] who compared the prediction from their model with radar data (from 1.2 GHz to 34.43 GHz) available in the community at this moment. The UD asymmetry from these measurements (see their figure 8) ranges from 1.0 to more than 2.2 in linear unit, depending on the incidence, polarization and frequency, whereas his model was only able to predict values from 1.0 to 1.7. There is also a large scatter in this comparison and the authors indicate that their model does not perfectly reproduce the upwind-to-downwind ratio features, although they adjust the relaxation time of the short waves to ensure compatibility between model and observations. This indicates that, by considering only the hydrodynamics effects due to straining of short Bragg waves, models can probably not reproduce all the UD asymmetry present in the data.

Some authors [*Bourlier*, 2004; *McDaniel*, 2003] try to explain the UD asymmetry of the radar backscatter through non-Gaussian statistics of the sea surface, without modeling the hydrodynamic process, which leads to such non-Gaussian statistics. They take into account skewness and kurtosis correlation functions, in addition to height and slopes correlation functions- as input in an electromagnetic model based on the small slope approximation. *Bourlier* [2004] finds an effect of skewness but only at small incidence angle where our data do not indicate a significant upwind-to-downwind asymmetry. *McDaniel* [2003] finds more effect but not in very good agreement with observations. The difficulty is that very little is known about the skewness and peakedness functions of the surface. Indeed, only *Cox and Munk* [1954] estimated slope probabilities involving statistics up to the fourth order - and only for points on the surface separated by a distance close to zero (see [*Bourlier*, 2004] for

instance). Thus, additional assumptions are needed to specify correlations functions for use in an electromagnetic model of radar cross-section.

KHCC introduced part of the upwind-to-downwind asymmetry by taking into account effects of wave breaking on the enhanced surface roughness. We will see below (section 5.1, 5.2) that indeed, we can confirm that the non-polarized part of the signal contributes quite significantly to the UD, which corroborates the idea that breaking waves are a major factor contributing to the UD asymmetry, even if we can not exclude other mechanisms like modulations of Bragg waves.

Concerning the UD ratio as a function of wind speed (Fig. 5a-b), the STORM observations show a clear increase with wind speed in both polarizations between 5 and 15 m s^{-1}, and a large scatter for the lowest wind speeds ($\leq$ 5 m s^{-1}). For wind speed above 5 m s^{-1}, the CMOD2-I3 and CMOD5 models (dashed-dotted lines with open stars and circles, respectively) also show an increasing trend of the UD with wind speed.

For the cases of light wind (< 5 m s^{-1}), the STORM data seem to indicate that the UD asymmetry decreases when wind speed increases. But, in this range of wind speed, there is not enough data to firmly conclude on the behavior of the upwind-to-downwind asymmetry. The TS+GO model (where we recall that hydrodynamic modulation effects are not included) gives a null (in dB) UD ratio (dashed lines). When the hydrodynamics effects are taken into account in the model (dotted lines) the trend with wind speed remains much too small compared to the experimental values – especially in HH polarization.

The same analysis has been performed for the UC asymmetry as a function of incidence and wind speed. Figure 6a-b shows the UC ratio for the STORM data (full circles) as a function of incidence in VV and HH polarizations for a wind speed of 10 m s^{-1} ($\pm$1 m s^{-1}). In both polarizations, the observed UC asymmetry increases with incidence angle. It is slightly larger in VV than in HH polarization. The empirical CMOD2-I3 and the CMOD5 models for the VV-polarization (dashed-dotted lines with open stars and with open circles respectively, in Figure 6a) also show an increase of the UC ratio with incidence. The CMOD5 function is very close to the STORM observations, whereas the CMOD2-I3 shows a weaker dependence with incidence, with an overestimate of the STORM results at incidence less than 25° and an underestimate at incidence larger than 32-35°. The TS+GO model (dashed lines) is in rather good agreement with the STORM data and the CMOD5 model (in VV) at incidence above 30°, whereas it overestimates the UC ratio of the CMOD2-I3 model in this incidence range. In HH-pol, the TS+GO model overestimates the STORM data. We will see below, that this drawback of the model cannot be compensated by introducing a non-polarized effect . Indeed, the analysis proposed in section 5.2 shows that the polarized part of the backscatter dominates the UC ratio. At incidences smaller than 30°, there is in opposite a slight overestimate (by 0.5 to 1 dB) of the TS+GO model compared to the experimental values of STORM (in VV and HH) and CMOD5 (in VV). In this range of incidence angle the UC ratio from the TS+GO model is very sensitive to the anisotropy of the long waves slopes which are imposed in the model through the angular distribution of empirical wave spectrum proposed by *Donelan et al.* [1985]. Shape of this spectrum is valid for the uniform conditions of wave generation, which are probably too idealized for the real maturate seas. Angular distribution of real maturate seas are broader, and this fact probably leads to overestimate the UC ratio at low incidence angle.

Figure 7 shows the UC ratio from STORM observations (full circles) versus wind speed for the incidence angle of 37.5° ($\pm$0.5°) in VV polarization. The CMOD2-I3 and CMOD5 models are shown as dashed-dotted lines with open star and open circle symbols, respectively. For the range of wind speeds between 5 and 15 m s^{-1}, both STORM and the empirical models show a clear increase of the UC ratio with wind speed. Although there are some differences between these experimental data sets, it is obvious that the TS+GO model (dashed lines) does not

exhibit a consistent trend with wind speed, even if the mean value seems in agreement with the observations. Indeed, for winds larger than 5 m s^{-1}, the trend of the UC ratio from the TS+GO model combined with the KHCC surface description is almost constant with wind speed, in contradiction with the increasing trend of the data. Similar results were obtained by *Kudryavtsev et al.* [2003] with an independent data set (their Fig.15b). Similar conclusions are also obtained for the HH polarization and at other incidences –not shown. When the ECKV97 surface model is used (dashed line with plus symbols), the agreement with the observations is not very good neither, but the trend is better: the UC ratio increases with wind speed but is underestimated with respect to the empirical values. This is due to the fact that the upwind to crosswind asymmetry of the waves in the Bragg wavenumber domain is slightly dependent with wind speed in the model of ECKV97, whereas it is almost independent of wind speed in KHCC. For the conditions of light winds (< 5 m s^{-1}), it is rather difficult to conclude, because of the small number of observations.

4.   Combination of dual polarization measurements

In this section we analyze the combination of polarizations (HH and VV) to better understand the surface properties, which influence the radar response.

Following the decomposition proposed in [*Quilfen et al.,* 1999], we consider that σ_0^p, the total NRCS in a given polarization (HH or VV indicated by the superscript *p*) expressed in linear units, can be decomposed through the following equation,

$$\sigma_0^p = \sigma^p + \sigma^{np} , \qquad\qquad (1)$$

where σ^p and σ^{np} are respectively the polarized and non-polarized contributions to the NRCS. This non-polarized contribution stands for the part of the NRCS that is not sensitive to the polarization (HH or VV).

By subtracting in linear units the NRCS in HH-pol to the NRCS in VV-pol, the non-polarized part can be removed:

$$\Delta\sigma = \sigma_0^{VV} - \sigma_0^{HH} . \qquad\qquad (2)$$

$\Delta\sigma$ contains only contribution from the polarized part of the signal. Note that the GO part is also removed by this operation.

Let us consider the asymmetry of this polarized part of the data:

$$\delta_{\varphi_1\varphi_2}^D = \frac{\Delta\sigma(\varphi_1)}{\Delta\sigma(\varphi_2)} \qquad\qquad (3)$$

where φ_1 and φ_2 reads for the directions (up-, down- and cross-wind) of the radar antenna with regard of the wind direction. For a given polarization, the asymmetry will be simply expressed as:

$$\delta_{\varphi_1\varphi_2}^p = \frac{\sigma_0^p(\varphi_1)}{\sigma_0^p(\varphi_2)} \qquad\qquad (4)$$

where superscript *p* is the considered polarization (VV or HH).

By analyzing the parameter $\Delta\sigma$, we present below a discussion on the validity of the model used to represent the polarized part of the signal and discuss the mechanisms, which could explain the UD and UC anisotropy of the radar cross-section in each polarization.

4.1.   Assessment of the model for polarized part of the backscatter

Below, we assess the polarized part of the signal by comparing experimental values of $\Delta\sigma$ to the model values. The model is the TSM as explained above and in the appendix, run with the surface wave spectrum from KHCC (or from ECKV97 for some comparisons). In the

electromagnetic part, we ignore hydrodynamic and breaking effects.

Figure 8 presents $\Delta\sigma$ in the upwind direction, versus incidence angle for a 10 m s^{-1} wind speed (± 1 m s^{-1}) . We observe that $\Delta\sigma$ decreases with incidence angle from 25° to 40°. The agreement between the model run with the spectrum of KHCC (solid line) and the observations is very good. Again, we recall that in $\Delta\sigma$ only the Bragg terms-modulated by the long waves slopes do not vanish. Hence, the comparison indicates that the polarized part of the NRCS versus incidence is well reproduced by the TSM with the KHCC surface spectrum. The comments are the same for wind speeds of 5 and 15 m s^{-1} (not shown).

Figure 9 presents $\Delta\sigma$ versus wind speed for the incidence angle of 37.5° (± 0.5°). The experimental values of $\Delta\sigma$ increase versus wind speed. The prediction of $\Delta\sigma$ from the TSM run with the KHCC surface spectrum (solid line) is again in very good agreement with the experimental data. This result is in fact quite normal since the sensitivity of the Bragg part of the backscatter is determined by the wind exponent n of the wave spectrum, which has been fitted here by using the experimental values of $\Delta\sigma$ (see annex, and KHCC).

Figure 10 shows $\Delta\sigma$ as a function of azimuth angle, at incidence 40.5° (± 0.5°) and for a case of high wind (14 m s^{-1}). It is clear from the data points, that the harmonic behavior of $\Delta\sigma$ is different from what was presented in figure 3 for each polarization: there is almost no upwind to downwind asymmetry. As $\Delta\sigma$ contains only information on the polarized radar signature, this indicates that the upwind to downwind asymmetry is mainly contained in the non-polarized part of the signal. The results of the TSM without considering hydrodynamic effects run with the KHCC surface description (solid line), is in good agreement with the observations, except that the UC ratio of $\Delta\sigma$ seems a little bit underestimated by the model.

Figure 11a shows the upwind to downwind ratio of $\Delta\sigma$ as a function of wind speed for 37.5°. It confirms that there is almost no asymmetry of $\Delta\sigma$ (values close to 1) whatever is the wind speed – whereas the UD is well pronounced in VV and HH-pol (see figures 5a and 5b). The model (containing only a polarized part) shows the same result. Hence, this analysis confirms that the upwind to downwind ratio of the total NRCS (Fig.5a) cannot be reproduced by a TSM which includes only a polarized contribution (at large incidence).

Figure 11b shows the upwind to crosswind ratio of $\Delta\sigma$ as a function of wind speed. The main trend is an increase with wind speed at winds stronger than 5 m s^{-1}. Compared to that, the TSM model run with the KHCC surface wave spectrum (solid line), shows almost no variation with wind speed (for winds larger than >5 m s^{-1}), which contradicts the observations. When the wave spectrum of ECKV97 is used (solid line with plus symbols), an increase of the upwind to crosswind ratio of $\Delta\sigma$ is found, but it is too weak compared to the observations, and the model still underestimates of the UC ratio of $\Delta\sigma$. Similar results have been obtained at other incidence (greater than 30°). Because we have used in this analysis, the difference of NRSC in VV and HH ($\Delta\sigma$) and not each NRCS in HH or VV, we may conclude that the reason of the discrepancy between model and data, also evidenced in Fig. 7, comes from a not fully appropriate angular description of the wind waves contributing to the polarized part of the electromagnetic model trough Bragg scattering mechanism.

As a summary on our results on the analysis of $\Delta\sigma$, we can conclude that the TSM model with the surface spectrum of KHCC used as input provides a very good representation of the polarized part of the NRCS as a function of wind speed and incidence (Figs. 8 and 9) and of the upwind to downwind ratio (Fig.10). In opposite the values and trend of δ^{D}_{UpCr} as a function of wind speed is not well reproduced by the model. This is due to the fact that the anisotropy of the Bragg waves in the surface model is almost constant with wind speed whereas the radar data show that this anisotropy should depend on wind speed. This is clearly a shortcoming of the KHCC model. The azimuth behavior is somehow better reproduced with the surface wave spectrum of ECKV97, because the surface spectrum of ECKV97 contains a dependence of the

upwind to crosswind asymmetry of the Bragg waves with wind speed (parameterized empirically). However, Fig. 11 clearly shows that this dependence is not sufficient to fully reproduce the data.

Analyzing the difference of polarization does not permit to conclude on the GO model used to complement the TSM at small incidence. But this was confirmed earlier in section 4. In particular, Figure 1 shows that GO model is valid to model the NRCS at low incidence angles where quasi-specular backscatter dominates. As a consequence we are confident in our combined model (TS+GO) used with the KHCC surface spectrum, at least for its dependence with wind speed and incidence. Concerning the azimuth behavior, we will further discuss the two options of using KHCC spectrum or the ECKV97 spectrum. Keeping this in mind, the TS+GO model will be used in section 6 to infer the non-polarized part of the NRCS.

4.2. Polarized and non-polarized mechanisms contributing to the surface anisotropy of the backscatter

In this section, only experimental data (no models) are used to assess some of the conclusions proposed in the previous section. We limit our analysis to the largest incidences ($\theta > 37.5°$) where the asymmetries are the most pronounced. Note that for these incidences, the so-called quasi-specular backscatter (responsible for the level of NRCS at small incidences) is negligible.

Figure (12a) shows a comparison between δ^D_{UpCr} and δ^{HH}_{UpCr}. Circles, diamonds and stars are respectively for incidence angles 37.5°, 40.5° and 42.5°. Open symbols indicate cases of wind speed higher than 10 m/s whereas full symbols are for lower wind speeds. Figure 12a shows a good agreement between δ^D_{UpCr} and δ^{HH}_{UpCr}, at least at low to moderate wind speed (≤ 10 m s^{-1}). As the effects of the non-polarized part of the NRCS are removed in δ^D_{UpCr}, we conclude that the UC asymmetry comes mainly from the polarized part of the signal, at least for wind speeds up to about 10 m s^{-1}. The results of *McDaniel* [2001] and *Voronovich and Zavorotny* [2000] using the SSA-2 model (only polarized effects), are consistent with this: they find that the UC asymmetry is very sensitive to the angular function chosen to describe the wave height spectrum. In Figure 12a, we note however that for the largest values of wind speed, the agreement between δ^D_{UpCr} and δ^{HH}_{UpCr} is not as good. In this case, the UC asymmetry is larger for δ^D_{UpCr} than for δ^{HH}_{UpCr}. As the non-polarized part contributes to δ^{HH}_{UpCr}, but not to δ^D_{UpCr}, we conclude that for these conditions, a non-polarized contribution should be invoked to decrease the upwind to crosswind asymmetry in HH (i.e. to represent an increase of the sea surface isotropy with wind speed). The conclusion are the same in VV polarization (not shown), although the deviation between δ^D_{UpCr} and δ^{VV}_{UpCr} is less.

In a similar way, Fig12-b presents a comparisons between δ^D_{UpDo} and δ^{HH}_{UpDo}. Note that the number of points in Fig12-b is about half the number of points in Fig12a, because there is only one upwind and one downwind direction, whereas there are two crosswind directions. Figure 12b shows that δ^D_{UpDo} differs from δ^{HH}_{UpDo} for almost all data points. It means that the non-polarized part of the NRCS (which is not included in δ^D_{UpDo}) contributes significantly to the UD asymmetry. We also observe that most of the values of δ^{HH}_{UpDo} are larger than those of δ^D_{UpDo}. It means that the non-polarized part of the NRCS increases the UD asymmetry. Hence we confirm, by analyzing observations without any assumptions on modeling, that the non-polarized part of the NRCS significantly affects the UD asymmetry. A similar effect is found in VV (not shown) although less marked. As for the UC asymmetry, the effect of the non-polarized part is strongest for the highest wind speeds.

4.3. Non polarized part of the NRCS

As shown above from comparisons with model and data and from data itself, a non-polarized contribution must be invoked to fully explain the behavior of the NRCS in both HH and VV polarizations – especially at high winds and large incidences. In this section, we propose an analysis of this non-polarized part for the measured NRCS as a function of wind speed, incidence and azimuth angle.

Using the formulation of the total NRCS expressed in Eq.(1), we now study the behavior of the non-polarized part of the signal, σ^{np}, removing from the measured NRCS (σ_{data}^{P}) the contribution represented by the TS+GO model ($\sigma_{\text{mod } el}^{P}$):

$$\sigma^{np} = \sigma_{data}^{P} - \sigma_{model}^{P}, \qquad\qquad (5)$$

where all the NRCS are expressed in linear units and the model $\sigma_{\text{mod } el}^{P}$ is used either with the KHCC surface spectrum or with the ECKV97 spectrum. The results presented below are obtained by choosing the horizontal polarization for the model and experimental values in Eq.(5) (superscript p=HH). We checked that the conclusions are similar when the VV polarization was used as an alternative.

Figure (13a) presents the results for σ^{np} versus incidence, in the upwind direction, for a wind speed of 10 m s^{-1}. Grey (respectively black) symbols in Fig.13a correspond to the case where the KHCC (respectively ECKV97) surface spectrum was used to estimate the polarized part. We observe that whatever is the surface spectrum used in the TS+GO model, the non-polarized part of the NRCS decreases with increasing incidence angles. This result is somewhat in contraction with the findings of *Plant* [2003] who assumes that the non-polarized part is due to diffusion by spherical droplets over the sea surface and is therefore non- dependent on incidence angle. In contrary, the decreasing trend of the non-polarized part with incidence is consistent with specular reflection due to enhanced roughness or larger mean square slopes of steep waves. Studies from *Voronovich and Zavorotny* [2001], *Ericson et al.* [1999] or KHCC (solid line in Fig.13a), suggest that this increase of roughness can be attributed to wave breaking processes. Figure (13b) and (13c) present the relative contribution of the non-polarized part of NRCS to the total NRCS (when the KHCC surface spectrum is used for the polarized part). We observe that for both polarizations, it increases with incidence angle. Moreover, this increase is larger in HH polarization, where the contribution to NRCS can reach 60% at 43°. The larger relative contribution in HH with respect to the case of VV explains that a model that does not take into account the non-polarized part (TS+GO model) performs rather well in VV but not in HH.

Figure (14) shows the non-polarized part of the NRCS versus wind speed in the upwind direction. The same symbols as in Fig.13a are used. As clearly evidenced in Fig.14, the non-polarized contribution increases with wind speed, whatever is the surface model considered in the polarized term (KHCC or ECKV97). Same results were obtained at all incidence angles greater than 30° (not shown). It means that the physical phenomena, which induce the non-polarized backscatter at large incidence, increases with wind speed as it was anticipated from our study with only data from STORM in section 5.2. Effects induced by wave breaking as proposed by KHCC – solid line in Fig.14*, or Voronovich and Zavorotny* [2001] is a good candidate for that, although density of droplets over the sea surface as invoked by *Plant* [2003] could also have the same effect, but would not be in agreement with the behavior with incidence shown in Fig.13.

Figure (15a) and (15b) present the non-polarized part of the NRCS versus azimuth angle for a case with a 14 m s^{-1} wind speed (Fig.15a using the KHCC, Fig.15b using the ECKV97 surface spectrum to estimate the polarized part). The vertical bar indicates the downwind direction. In opposite to the cases of the total NRCS or of the polarized part, there is here,

only one clear maximum and it occurs in the upwind direction. This is found whatever is the surface spectrum used to estimate the polarized part (compare Fig15a and 15b). This is in agreement with our asymmetry analysis in section (4) where we suggested that the non-polarized part of the NRCS should play a role in the UD asymmetries. According to our analysis this non-polarized contribution will tend to increase the UD asymmetry of the total NRCS.

As a summary of Sections 4 and 5, we may conclude that in order to fully explain the observations in both polarizations we need to consider a contribution of non-polarized backscatter to the total NRCS. This contribution is dependent on wind speed and direction, as well as on the incidence angle. This confirms the model approach developed by KHCC for the non-polarized part.

5.   Model for the total NRCS in the dual polarization configuration

The model proposed to estimate the NRCS in HH and VV polarization in all configurations of wind speed (2 to 20 m s^{-1}), incidence (0 to 45°) and azimuth angles (0 to 360°) is basically the same as the one presented in KHCC, except for slight changes (see appendix).

The polarized part was already presented above. The main changes with respect to the model of KHCC are that i) we ignored the effect of hydrodynamic modulation of Bragg waves on the NRCS, ii) the wind exponent of the wave spectrum has been slightly changed (see Appendix). The non-polarized part is similar to KHCC except for one constant ($\overline{\theta_{wb}}$ in Eq. A3, see appendix). It describes the contribution of specular reflection -assumed to be similar in both HH and VV polarizations- from breaking zones characterized by enhanced surface roughness (see appendix). As discussed above, the non-polarized part of the model (solid lines in Figs13a, 14 and 15) is in good agreement with the non-polarized part derived from the observations (see section 5), except for the case of low wind speed. The model results for the total NRCS (summing the polarized and non-polarized part) in HH and VV polarization are presented in Figures 1 to 7 as solid lines.

Figure 1 shows that with this model, the variation of the NRCS with incidence angle is well reproduced in both VV and HH, in opposite to the case when the TS+GO model was used. As a consequence, the polarization ratio as a function of incidence angle (Figure 16a) is also well reproduced by the model. In opposite, the TS+GO model overestimates the polarization (dashed line in Fig.16a). At 40° incidence this overestimation reaches about 2 dB.

Figure 2 shows that the agreement between the full model (solid line) and our observations for the variation of the NRCS with wind speed is also much better than with the TS+GO model (dashed line). The sensitivity to wind speed is well reproduced, although the model still underestimates both the STORM observations and the CMOD models at low wind speeds. This underestimate might be due to a combination of several approximations like neglecting wind variability in the cases of light winds [*Plant*, 2000] or other sea surface phenomena like current, or slicks. But it cannot be attributed to the breaking waves, because of their minor contribution at light wind. In terms of polarization ratio (VV/HH), Figure 16b shows that both the observations and the model indicate only a slight wind dependency. The trend with wind speed is not very different with the TS +GO model (dashed line in Fig.16b), which also shows a slight decrease of the polarization ratio with wind speed, but with an overestimate of the polarization ratio at all wind speeds.

Figure 3 shows that the full model reproduces also quite well the azimuth behavior of the NRCS both in HH and VV polarizations (solid line in Fig.3). The improvement with respect to the TS+GO model is particularly important for the HH polarization (Fig3b). The upwind to downwind anisotropy is now well reproduced and the mean level is also in agreement with the data. An assessment of the role of wave breaking on the UD asymmetry is also given by the

statistical analysis of the NRCS in the upwind and downwind directions. Indeed, for the experimental conditions of Fig.3, the normalized standard deviation of the HH-NRCS (standard deviation divided by the mean value in linear units) is larger in the upwind direction than in the downwind direction (respectively 28 and 21%). This is compatible with the proposed scattering model which predicts that wave breaking events at sea surface will contribute more strongly in upwind than in downwind direction.

The ability of the full model to reproduce the observed azimuth variation of the NRCS in HH- and VV- polarizations is also illustrated by Figure 16c, which shows the polarization ratio (VV/HH expressed in dB) as a function of azimuth. The full model reproduces very well the first maximum of the polarization ratio in the downwind direction, and the second one in the upwind direction. In opposite, the TS+GO model dashed line in Fig.16c) exhibits almost no upwind to downwind asymmetry.

We look now in more details at the azimuth behavior of the NRCS. The variation of the upwind-to downwind ratio with incidence angle and wind speed is well reproduced by the model in HH and VV (Figure 4a-b and 5a-b, solid line), although the hydrodynamic effects in the polarized part of the model have been omitted. Indeed, all the upwind to downwind asymmetry is due here to the effects of the steep breaking waves on the signal. This is likely an upper limit for this effect, but we have shown above (see comments on Figures. 10, 11a and 12b) that the hydrodynamic effects on the Bragg scatters are surely not sufficient to explain the UD asymmetry. The full model is also in rather good agreement with the empirical CMOD models for the VV polarization (dashed-dotted lines with open stars and circles in Figs.4a and 5a). Even if there are some differences between the different sources of data, it is clear that only the full model is able to predict an increase of the UD asymmetry with wind speed and incidence angle. The ability of the full model to reproduce the observed variation of the UD asymmetry NRCS in HH- and VV- polarizations is also illustrated by Figure 16d, which shows the downwind to upwind ratio of polarization ratio (VV/HH), as a function of incidence. The full model reproduces very well the increase of this ratio for incidence angles larger than 30°. In opposite, the TS + GO model (dashed line in Fig.16d) exhibits almost no increase with incidence.

The results for the upwind to crosswind ratio versus incidence (Figure 6a-b), show that introducing the wave breaking effects (solid lines) decreases the upwind to crosswind ratio at the largest incidence angles compared to the results obtained with the TS+GO model (dashed lines). This decrease when the full model is used is due to the fact that wave-breaking effects tend to make the surface more isotropic. The agreement with the STORM observations and the CMOD5 model is degraded, compared to the case when the sole polarized effect is taken into account (TS+GO model-dashed lines). However in VV-polarization, the agreement of the full model with the CMOD2-I3 empirical model is rather good.

Finally for the upwind to crosswind ratio as a function of wind speed (Fig.7), the trend found with the full model using the surface wave spectrum of KHCC (solid line), is not in better agreement with the STORM data nor with the CMOD models, than when the TS+GO model was used (dashed line): it gives a decreasing trend with wind speed for winds larger than about 5 m s^{-1}, whereas the observations show an increase in this range. Indeed, adding breaking effects (as in the full model) cannot correct the deficiencies of the polarized part of the model already evidenced as in Fig.11b for example. When using the ECKV97 surface spectrum in the full electromagnetic model (solid line with plus symbols in Fig.7) gives a slightly better agreement. In this case, the agreement between model and data for the polarized part (dashed line with plus symbols in Fig. 7) was better.

6.   Conclusion

In this study, we have combined the analysis of radar observations in two polarizations, and models of different kinds to study some of the ocean surface properties and their relation with the ocean surface backscatter. One of the most striking results concerns the anisotropy of the surface. Indeed, we have shown that:

- The upwind to downwind anisotropy of the radar signal cannot be explained entirely by the modulation of Bragg waves by longer surface waves. Specular reflection from zones with enhanced roughness associated with breaking waves add a non-polarized contribution to the signal, and may be invoked to explain the upwind to downwind anisotropy (at least when $U >$ 5 m s^{-1}).

- The upwind to crosswind anisotropy of the surface increases with the incidence angle. At moderate incidence such behavior is associated with a narrowing of wave spectrum for increasing wave number of Bragg waves. The KHCC model of wave spectrum based on the energy balance equation reproduces this trend.

- Observed upwind to crosswind anisotropy of the sea surface increases with wind speed (at $U >$ 5 m s^{-1}). The model of KHCC cannot reproduce this trend. In a complementary test, wind direction variability as was observed and parameterized by *Carswell et al.* [1999] was introduced into the KHCC model. However this modification did not change significantly the results on upwind to crosswind anisotropy (not shown). At C-Band, taking into account the generation of parasitic capillary waves by non-linear effects (as done here) is not sufficient neither, to explain the observed upwind to crosswind asymmetry. Taking into account other non-linear wave-wave interactions that redistribute wave energy in the wavenumber space, could probably improve the model in terms of up- to cross-wind anisotropy versus wind speed (see *Caudal* [2002]). This will be tested in the future. Model simulation based on the empirical wave spectrum of EKCV97 gives slightly better results, but the agreement is still not good.

- At light wind (< 5 m s^{-1}), discrepancy between the model predictions and observations is obvious, for almost all scattering properties of the sea surface. On the one hand, there is a number of factors which are not accounted for, but may significantly affect the results, in particular, (i) spatial and temporal heterogeneity of wind field which may influence both waves near the spectral peak (making them different from the idealized Donelan et al spectrum adopted in the present study), and short wind waves (see, e.g. [*Plant*, 2000]); (ii) local features of the surface currents which may affect wind waves through wave-current interaction and result in suppression of short wind waves by surfactants accumulated in the current convergence zones. These processes will dominate in the cases of light winds whereas the breaking effects are negligible.

In this study, Gaussian properties of the surface were assumed. Another way of analyzing surface properties and their impact on the radar signal could be to account for non-Gaussian effects in an electromagnetic model, which could take into account high order statistics of the surface (correlation function). Models based on the Small Slope Approximation [*Voronovich*, 1994] or on the Weighted Curvature Approximation [*Elfouhaily et al.*, 2003] are good candidates to test this point. Moreover, we could think of linking up our work to the non-Gaussian statistic properties of the sea surface. Indeed, the specular and the non-polarized terms could be rewritten in only one expression with mean square slopes different than the one of a regular surface. In that sense, parts of the sea surface considered regular would be characterized by the classical mss whereas pattern containing enhanced roughness associated with breaking waves will be associated with different values of mss varying from one pattern to another. This approach leads to a so-called compound model (see Chapron et al.) to describe the surface (at least from moderate to high wind where waves breaking effects exist) which enables to take into account the non-Gaussian properties of the sea surfaces and could be beneficial to reproduce the NRCS level. Future work should be devoted understand these

problems for the statistical representation of the sea surface.

Another important result of the study is that, by combining a two-scale model and observations in two polarizations, we could assess the effect of non-polarized backscatter on the total NRCS and present its characteristics. This non-polarized backscatter decreases with incidence and increases with wind speed with trends consistent with the model proposed by *Kudryavtsev et al.* [2003]. Hence, this study validates the model of the non-polarized part, which is assumed related to the scattering from zones of enhanced roughness associated with breaking waves. Overall, the non-polarized contribution may reach up to 60% of the total backscatter in HH polarization at large incidence angle.

The proposed full model, which takes into account the non-polarized contribution over breaking zones gives good agreement at the same time with i) the observed polarization ratio, ii) the NRCS in each polarization and its variation with incidence, wind speed (for winds above 5 m s^{-1}) and azimuth.

This analysis was however limited to C-Band radar data, and further work with other radar bands should be done in order to generalize the conclusions.

Appendix: Model of Radar backscatter

We use here a slightly modified version of the model of the NRCS proposed in *Kudryavtsev et al.* [2003] (also referred as KHCC). The sea surface is represented as a "regular" (non-breaking) wavy surface combined with a number of breaking zones of enhanced roughness (*Kudryavtsev et al.* [2003]). Note that definition of enhanced roughness associated with wave breaking includes various patterns like slope of actively spilling breakers, "rough" surface of a plume breaker, "turbulent" wake of breaking, enhanced/disturbed surface left by a broken wave crest, etc. Radar scattering from the regular surface and the wave breaking zones are statistically independent, thus the NRCS is presented as a sum of two terms:

$$\sigma_0^p = \sigma_{0R}^p (1-q) + \sigma_{0b} q \qquad (A1)$$

where q is the fraction of the sea surface covered by zones of enhanced roughness associated with breaking waves, and σ_{0R}^p and σ_{0b} are the NRCS of the regular surface and of the zones of enhanced roughness respectively. Nevertheless, it must be noted that q does not represent the fraction of the sea surface covered by foam coverage and air bubbles visible with an optical sensor. Moreover, as we mentioned below, q characterizes various patterns associated with breaking wave which explains that our q parameter is greater than the one given in literature to characterize zones with spilling breakers or foam coverage. There is no experimental documentation of this fractional area on the sea surface for a given wind speed. Finally, we also recall that the non-polarized term of the model was established in agreement with the work of *Ericson et al.* who showed that specular reflection dominates at least over 30% of the distance along the breaking wave profile (see their figure 9) which is much larger than the one occupied by active spilling breakers.

a) Backscattering from the regular surface.

As in the KHCC, σ_{0R}^p is described as a standard composite model combining two asymptotic solutions, the 2-scale Bragg scattering, and the geometrical optics approximation (e.g. *Valenzuela et al.* [1971], *Thompson* [1988]). In the composite models, the wave spectrum is divided in two intervals, small-scale waves $k > k_d$ and large-scale waves $k < k_d$. In our study we define $k_d = k_r /4$ as was used in *Voronovich and Zavorotny* [2001]. Small-scale waves provide resonant scattering, while large-scale waves affect the Bragg scattering via random changes in the local incidence angle and rotation of the incidence plane. At small

incidence angle, large-scale waves also contribute to specular reflections.

In the KHCC model, the two-scale Bragg model was expanded in Taylor series up to the 2nd order. This approach allowed taking into account effect of Bragg waves modulations on the NRCS. However, this expansion looses its validity at incidence angles less than about 25° , which is not appropriate for the analysis of our data. Therefore in the present study we use the 2-scale Bragg model in its standard form (via integral with PDF for the tilting waves), ignoring the effect of hydrodynamic modulations (except for one test shown in Figs.4-5) .

b) Backscattering from wave breaking zones

The second term in (A1) describes the contribution of wave breaking zones to the sea surface NRCS. As suggested in KHCC, the radar scattering from an individual breaking zone can be described as specular reflections from very rough wave breaking patterns, and only breaking of waves with wavenumbers much less than the electromagnetic wave number k_r (10 or more times less) contribute to the radiowave scattering. As in KHCC, we assume that the NRCS of an individual wave-braking zone can be described by quasi-specular reflection and reads:

$$\sigma_{0wb}(\theta) \propto (\sec^4\left(\theta - \theta_{wb}^i\right)/s_{wb}^2)\exp\left[-\tan^2\left(\theta - \theta_{wb}^i\right)/s_{wb}^2\right] + \varepsilon_{wb}/s_{wb}^2 \tag{A2}$$

where θ_{wb}^i is the tilt of breaking zone in the incidence plane, s_{wb}^2 is the mean square slope of the breaking zone roughness (which is assumed isotropic), ε_{wb} is the ratio of vertical to horizontal scale of the breaking zone. The proportionality coefficient implied in (A2) is an effective Fresnel coefficient for the breaking zone. The first term in (A2) describes the specular reflection from the enhanced roughness inside a breaking zone, while the second term describes reflection from the side of a breaking zone. It was suggested that θ_{wb}^i has the same mean value $\overline{\theta_{wb}}$ for all breaking zones. Then the tilt of a breaking zone in the incidence plane is $\theta_{wb}^i = -\overline{\theta_{wb}}\cos(\varphi - \varphi_1)$, where φ is the radar look direction, and φ_1 is the direction of propagation of a breaking wave. Averaging over the angular distribution of the wave breaking fronts, Λ_φ, the NRCS of each breaking zone is given by:

$$\sigma_{wb}(\theta,\varphi) = \frac{\int \sigma_{0wb}\left[\theta + \overline{\theta_{wb}}\cos(\varphi - \varphi_1)\right]\Lambda_\varphi(\varphi_1)d\varphi_1}{\int \Lambda_\varphi(\varphi_1)d\varphi_1} \tag{A3}$$

$\overline{\theta_{wb}}$ is fixed in this study to a value 0.08 instead of 0.05 in KHCC to reproduce the observed dependence of the upwind to downwind ratio a as a function of incidence angle in absence of hydrodynamic modulation (Fig. 4).

The total contribution of breaking waves (second term of Eq.A1) is :

$$\sigma_{0b}\ q = \sigma_{wb}(\theta,\varphi)c_q \int_\varphi \int_{k<k_{wb}} \Lambda(k,\varphi)dkd\varphi \tag{A4}$$

where k_{wb} is the wavenumber of the shortest breaking waves providing specular reflection (chosen as $k_r/10$), c_q is a constant, $\Lambda(k,\varphi)$ is the 2D distribution of wave breaking fronts (see below), and $\sigma_{wb}(\theta,\varphi)$ is given by Eq.(A3).

Values of the c_q, s_{wb}^2, ε_{wb} coefficients in (A2, A4) are taken here as proposed in KHCC, who tuned this coefficients so as to fit available radar observations in the literature at various wavelengths.

A2. Surface Waves

Using the electromagnetic model as presented above requires defining the wave number

spectrum (wave height and/or wave curvature). The spectrum is chosen as in KHCC, as the weighted sum of a the wave number spectrum in the equilibrium range (far from the peak of the spectrum), $S_h(k,\varphi)$, and of the wave number spectrum near the peak of the spectrum, $S_l(k,\varphi)$:

$$S(k,\varphi) = S_l(k,\varphi)\exp(h) + S_h(k,\varphi)(1-\exp(h)) \qquad (A5)$$

where the exponential terms are used to cutoff the contributions of S_l at large wave numbers and of S_h at low wavenumbers. The expression of h was chosen following *Elfouhaily et al.* [1997]. In the following the curvature spectrum $B_l(k,\varphi)$ and $B_h(k,\varphi)$ are also used. They are related to the wave height spectrum by:

$$B(k,\varphi) = k^4 S(k,\varphi) \qquad (A6)$$

a) Spectrum of wind waves in the equilibrium range

As in KHCC, the wave spectrum in the equilibrium range of wind waves (far from the spectral peak) is expressed as a solution of the energy balance equation accounting for the wind energy input, viscous dissipation, non-linear energy losses due to wave breaking, and generation of parasitic capillaries. Outside the range of capillary waves (which do not contribute to radar response in C-Band), the wave spectrum is:

$$B_h(k,\varphi) = \alpha\left[\left(\beta_\nu(k,\varphi)\right)\right]^{1/n} \qquad (A7a)$$

with

$$\beta_\nu(k,\varphi) = \left(C_\beta \frac{u_*^2}{c^2} - \frac{4\nu k^2}{\omega}\right)\exp\left[-(\varphi-\varphi_w)^2\right] \qquad (A7b)$$

where $\beta_\nu(k)$ is the effective growth rate, C_β is a growth rate parameter, u_* the air friction velocity, c the phase velocity, ν the viscosity coefficient, φ_w direction of wind velocity. The dispersion relation links the frequency ω and the wavenumber k.

Parameters α and n in (A7a) are the main model parameters and defined by Eq.(22) and (26) in KHCC. They are functions of k/k_γ (where $k_\gamma = (g/\gamma)^{0.5}$ and g and γ are the gravity acceleration and surface tension, respectively), and equal to constants $\alpha = \alpha_g$, $n=n_g$ at $k/k_\gamma \ll 1$ and equal to $n=1$ in the vicinity of the minimum phase velocity, at $k/k_\gamma \approx 1$. Quantity $\frac{2}{n(k/k_\gamma)}$ corresponds to the wind exponent of the wave spectrum. A « filter » function is defined to link the limit value at $k/k_\gamma \ll 1$ to the limit value at $k/k_\gamma \approx 1$. In KHCC, the coefficients of this filter function were tuned to obtain an agreement wind exponents of the NRCS in VV (assuming pure Bragg backscatter) deduced from various published radar data sets at different wavelengths. Here, instead, we have used the difference of polarization (VV-HH) to suppress any possible non-polarized contribution of the signal. The revised model of wind exponent is shown in Fig. A1, with the experimental data superimposed. The corresponding coefficients are $k_l=2$, $k_h=10$. Note that after this minor modification the wind exponent becomes very close to the one proposed by *Trokhimovski and Irisov* [2000].

b) Spectrum of dominant waves

B_l is chosen here as the empirical spectrum of *Donelan et al.* [1985] assuming infinite fetch.

c) Wave breaking front statistics

Equations A3-A4 are expressed in terms of the length of wave breaking fronts per unit area

and per unit wavenumber, $\Lambda(k,\varphi)d\varphi dk$. From the dimensional arguments proposed by *Phillips* [1985]) based on the experimental results of *Duncan* [1981], and assuming a power relation between the dissipation rate by breaking and the curvature spectrum normalized by a threshold, KHCC express $\Lambda(k,\varphi)$ as:

$$\Lambda(k,\varphi) \quad = \quad \frac{1}{2k}\left(\frac{B_h(k,\varphi)}{\alpha}\right)^{n+1} \qquad (A11)$$

Hence, with this approach, the fraction of sea surface covered by breaking waves contributing to the radar signal, q in Eq. (A1 or A4), and the NRCS of the breaking waves, σ_{wb} (Eq.(A3)) are both parameterized in terms of the wave curvature spectrum in the equilibrium range.

References
Banner M. L., Equilibrium spectra of wind waves *J. Phys. Oceanogr.* **20** 966–84, 1990.

Bentamy A., Y. Quilfen, P. Queffeulou, A. Cavanie, Calibration of the ERS-1 scatterometer C-band model, *Tech. Rep. DRO/OS-94-01*, 72 pp., Inst. Fr. Rech. Pour l'Exploit. de la Mer, Brest, France, 1994.

Bourlier C., Azimuthal harmonic coefficients of the microwave backscattering from a non-Gaussian ocean surface with the first-order SSA model, *IEEE Trans. on Geoscience and Remote Sensing*, 42, (21), 2600-2611, 2004.

Carswell J.R., W.J. Donnely, R. E. McIntosh, M.A. Donelan, and D.C. Vandemark, Analysis of C and Ku band ocean backscatter measurements under low-wind conditions , *J. Geophys. Res.*, vol. 104 (C9), 20,587-20,701, 1999.

Caudal, A physical model for the narrowing of the directional sea wave spectra in the short gravity to gravity-capillary range, *J. Geophys. Res.*, 107(C10), doi:10.1029/2000JC000437, 2002.

Cox C., and W. Munk, Measurements of the roughness of the sea surface from photograms of the sun's glitter, *J. Opt. Soc. Am.*, 44, No11, 1954.

Donelan M., J. Hamilton, and W.H. Hui, Directional spectra of wind-generated waves, *Philos. Trans. of the Royal Soc. Of London*, A315, 509-562, 1985.

Duncan J.H., An experimental investigation of breaking waves produced by towed hydrofoil, *Proc. R. Soc. London*, Ser. A, 377, 331-348, 1981.

Elfouhaily, T., B. Chapron, K. Katsaros, and D. Vandermark, A unified directional spectrum for long and short wind driven waves, *J. Geophys. Res.*, 102, C15, 15,781-15,796, 1997

Elfouhaily T., S. Guignard, R. Awadallah, and D.R. Thompson, Local and non-local curvature approximation : a new asymptotic theory for wave scattering, *Waves in Rand. Media*, 13 (4), 321-37, 2003.

Ericson, E.A., D.R. Lyzenga, and D.T. Walker, Radar backscattering from stationary breaking waves, *J. Geophys. Res.*, 104, C12, 29,679-29,695, 1999.

Hauser D., T. Podvin, M. Dechambre, R. Valentin, G. Caudal and J-F. Daloze, "STORM: A New Polarimetric Real Aperture Radar for Earth Observations," in *Proc. of the POLinSAR Workshop on applications of SAR polarimetry and polarimetric interferometry, organized by ESA/ESRIN*, 14-16 January 2003, Frascati.
Available: http://earth.esa.int/polinsar/participants/hauser4/POLINSAR-STORM.pdf

Hersbach H., CMOD5 an improved geophysical model function for ERS C-band scatterometry, *Techn. Mem.*, ECMWF, Reading, UK, 2003.

Kudryavtsev V., D. Hauser, G. Caudal, B. Chapron, A semi-empirical model of the normalized radar cross section of the sea surface, 1.Background model, *J. Geophys. Res.*, Vol. 108 No. C3, 10.1029/2001JC001003, 2003.

McDaniel, S.T., Small-slope predictions of microwave backscatter from the sea surface, *Waves in Rand. Media*, 11, 343-360, 2001.

McDaniel S.T., Microwave backscatter from non-Gaussian seas, *IEEE Trans. Geoscience. Remote Sens.*, 41(1), doi 10.1109/TGRS.2002.808069, 2003.

Mouche A., D. Hauser, J-F. Daloze, and C. Guérin, "Dual Polarization Measurements at C-Band over the Ocean: Results from Airborne Radar Observations and Comparison with ENVISAT ASAR data", *IEEE Trans. Geosci. Remote Sens.*, 43(4), 753- 769, 2005.

Phillips, O.M., Spectral and statistical properties of the equilibrium range in the wind-generated gravity waves, *J. Fluid Mech.*, 156, 505-531, 1985.

Phillips, O.M., Radar returns from the sea surface - Bragg scattering and breaking waves, *J. Phys. Oceanogr.*, 18, 1063-1074, 1988.

Plant, W.J., A two-scale model of short wind-generated waves and scatterometry, *J. Geophys. Res.*, 91, C9, 10,735-10,749, 1986.

Plant, W.J., Bragg scattering of electromagnetic waves from the air/sea interface, in *Surface Waves and Fluxes*, Volume II - Remote Sensing, 41-108, 1990.

Plant W.J., W.C. Keller, V. Hesany, T. Hara, E. Bock, and M. Donelan, Bound waves and Bragg scattering in a wind-wave tank, *J. Geophys. Res.*, 104(C2), 3243-3263, 1999.

Plant W.J., Effects of wind variability on scatterometry at low wind speeds, *J. Geophys. Res.*, 105 (C7), 16,899-16,910, 2000.

Plant W.J., Microwave Sea Return at Moderate to High Incidence Angles, *Waves Rand. Media*, vol. 9, pp. 339-354, 2003.

Quilfen Y., B.Chapron, A.Bentamy, J.Gourrion, T.M.Elfouhaily, D.Vandermark, Global ERS 1 and 2 NSCAT observations: Upwind/crosswind and Upwind/downwind measurements, *J. Geophys. Res.*, (104), 11,459-11,469, 1999.

Romeiser R., W. Alpers, and V. Wismann, An improved composite surface model for the radar backscattering cross-section of the ocean surface. Part 1: Theory of the model and optimization/validation by scatterometer data, *J. Geophys. Res.*, 102(C11), 25,237-25,250, 1997.

Thompson D.R., Calculation of radar backscatter modulations from internal waves, *J. Geophys. Res.*, 91(C10), 12,371-12,380, 1988.

Trokhimoski Y.G., and V.G.Irisov, The analysis of wind exponents retrieved from microwaves radar and radiometric measurements, *IEEE Trans. Geosci. Remote Sens.*, 18, 470-479, 2000.

Valenzuela, G. R., Theories for the interaction of electromagnetic and ocean waves - A review, *Bound. Layer Met.*, 13, 61-85, 1978.

Valenzuela, G. R, M.B. Laing, and J.C. Daley, Ocean spectra for the high frequency waves as determined from airborne radar measurements, *J. Mar. Res.*, 29(2), 69-84, 1971.

Voronovich A.G., Small-slope approximation for electromagnetic wave scattering at a rough interface of two dielectric half-spaces, *Waves Rand. Media*, 4, 337-367, 1994.

Voronovich A.G., V.U. Zavorotny, and V.G. Irisov, Sea-roughness spectrum retrieval from radar and radiometric measurements, *Proc. Int. Geosci. Remote Sens. Sympo. (IGARSS-2000, Honolulu, HI)*, Vol VII, Ed. TI Stein (Piscataway, NJ:IEEE), 1495-1497, 2000.

Voronovich A.G. and V.U. Zavorotny, Theoretical model for scattering of radar signals in K_u- and C-bands from a rough sea surface with breaking waves, *Waves Rand. Media*, 11, 247-269, 2001.
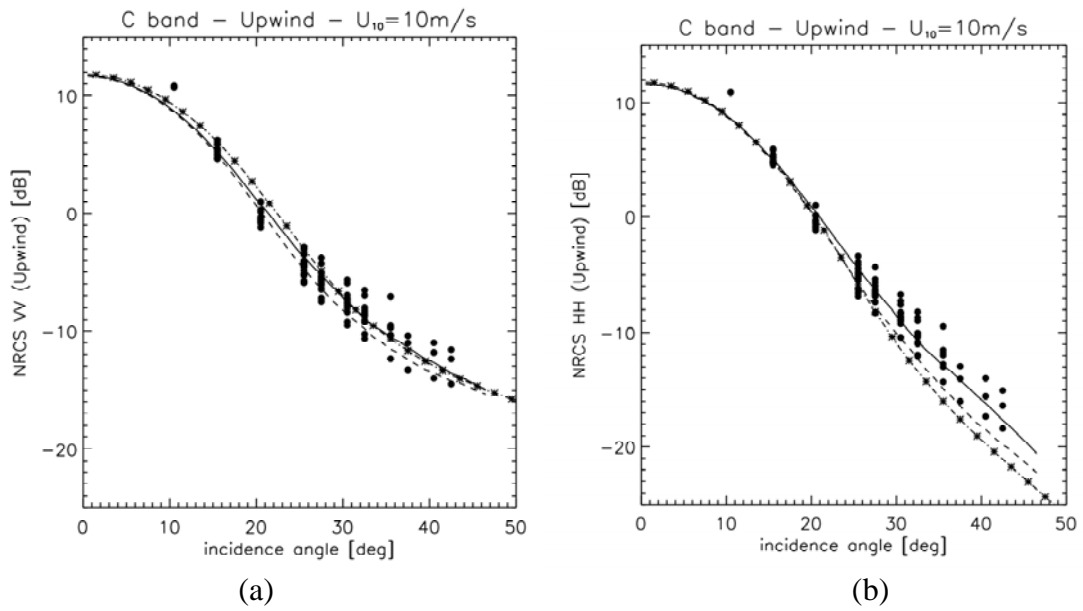
Figure 1: Normalized radar cross-section in VV (a) and HH (b) polarizations, as a function of incidence angle and for a 10 m s⁻¹ wind speed. The STORM observations in C-Band are plotted as black dots. The TS+GO model using the spectrum of KHCC is plotted as a dashed line. The dashed-dotted line with star symbols corresponds to the SSA-1 model with the same surface spectrum. The solid line corresponds to the full electromagnetic model, including a non-polarized contribution due to breaking waves.
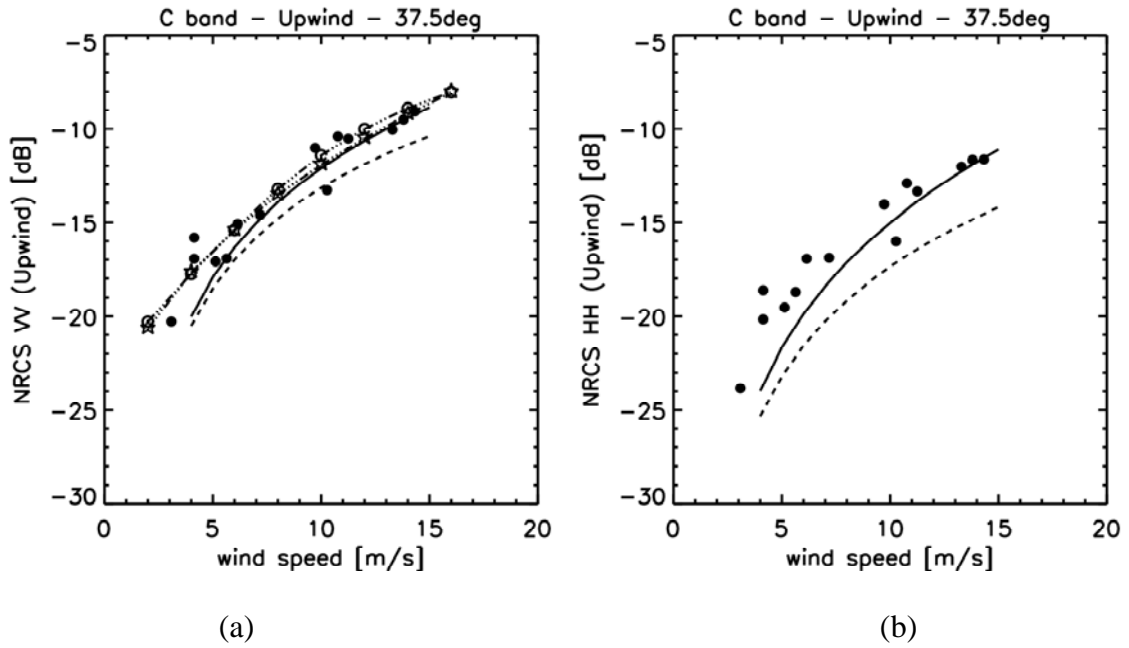
Figure 2: Normalized radar cross-section in VV (a) and HH (b) polarizations, as a function of wind speed for the incidence angle of 37.5°. The STORM observations in C-Band are plotted as black dots. The empirical CMOD2-I3 and CMOD5 models are shown as dashed-dotted lines with open star and open circle symbols, respectively. The TS+GO model using the spectrum of KHCC is plotted as a dashed line. The solid line corresponds to the full electromagnetic model, including a non-polarized contribution due to breaking waves.
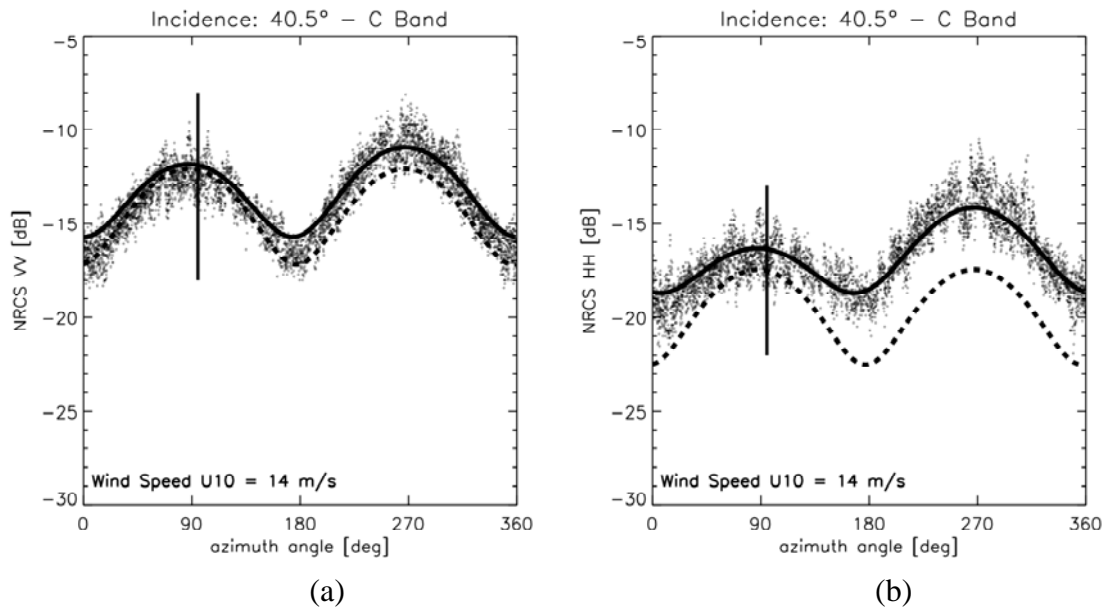
Figure 3: Normalized radar cross-section in VV (a) and HH (b) polarizations, as a function of the azimuth angle, for the incidence angle of 40.5° in a case of a strong wind speed (14 m s^{-1}). The symbols refer to the STORM data. The TS+GO model using the spectrum of KHCC is plotted as a dashed line. The solid line corresponds to the full electromagnetic model, including a non-polarized contribution due to breaking waves. The vertical bar indicates the downwind direction.
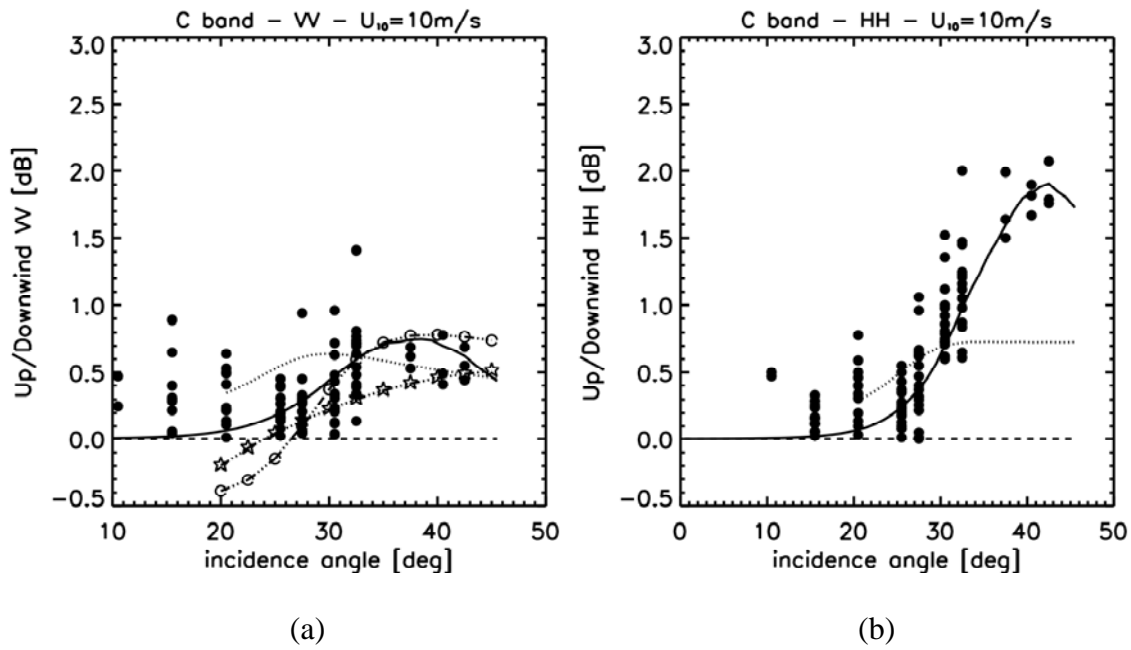
Figure 4: Upwind to downwind ratio (in dB) of the NRCS in VV (a) and HH (b) polarizations as a function of incidence angle for a 10 m s^{-1} wind speed. The STORM observations in C-Band are plotted as black dots. In Fig.4a, the empirical CMOD2-I3 and CMOD5 models are shown as dashed-dotted lines with open star and open circle symbols, respectively. The TS+GO model using the spectrum of KHCC, is plotted as a dashed line (respectively dotted line) when the hydrodynamic modulation of the Bragg waves is (respectively is not) taken into account. The solid line corresponds to the full electromagnetic model, including a non-polarized contribution due to breaking waves.
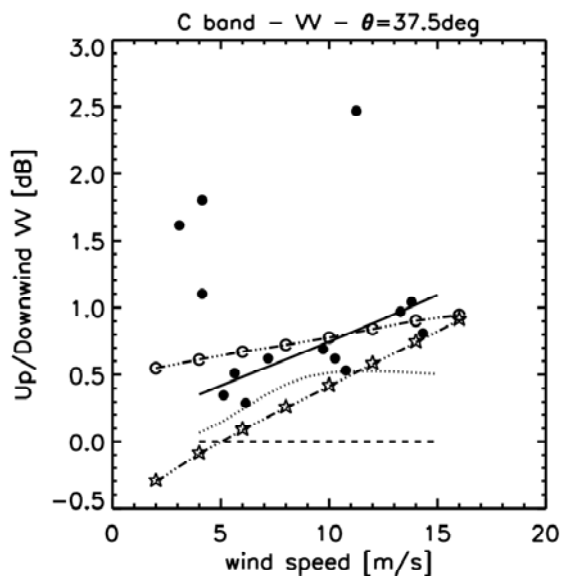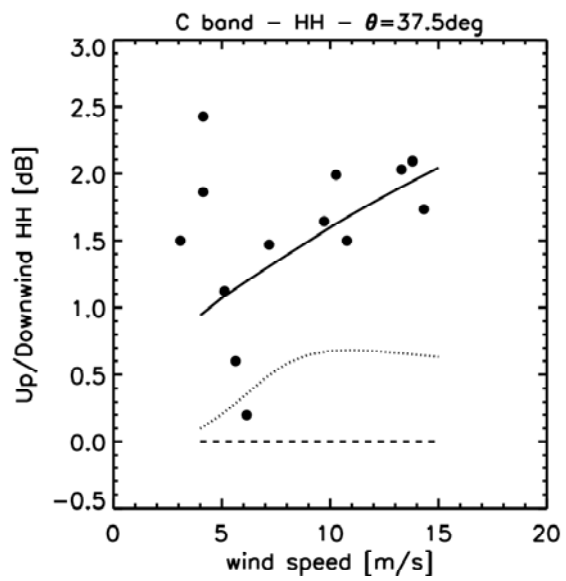
Figure 5: Same as in Figure 4, but for the upwind to downwind ratio (in dB) as a function of wind speed, for the 37.5° incidence angle.

(a)　　　　　　　　　　　　　　　　　(b)
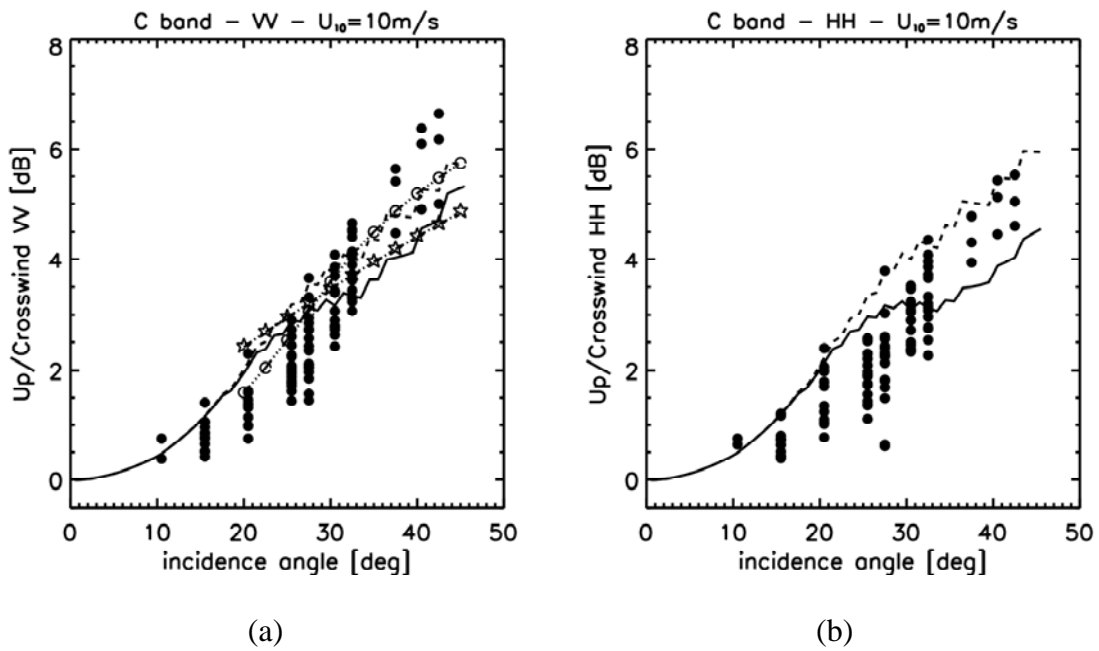
Figure 6: Upwind to crosswind ratio (in dB) of the NRCS in VV (a) and HH (b) polarizations as a function of incidence angle for a 10 m s^{-1} wind speed. The STORM observations in C-Band are plotted as black dots. In Fig.6a, the empirical CMOD2-I3 and CMOD5 models are shown as dashed-dotted lines with open star and open circle symbols, respectively. The TS+GO model using the spectrum of KHCC, is plotted as a dashed line. The solid line corresponds to the full electromagnetic model, including a non-polarized contribution due to breaking waves.
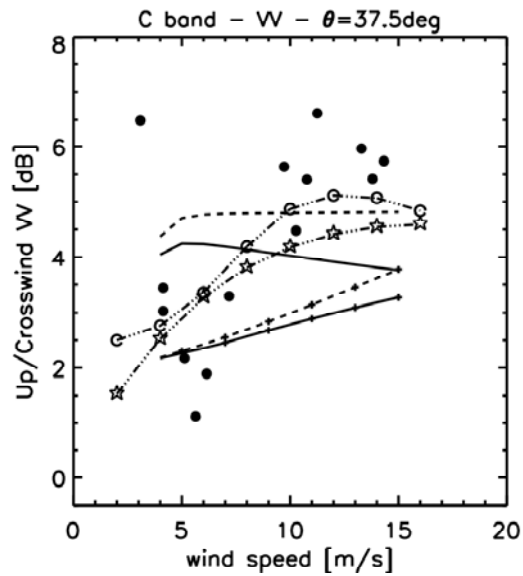
Figure 7: Upwind to crosswind ratio (in dB) of the NRCS in VV as a function of wind speed for the 37.5° incidence angle. The STORM observations in C-Band are plotted as black dots. The empirical CMOD2-I3 and CMOD5 models are shown as dashed-dotted lines with open star and open circle symbols, respectively. The TS+GO model is plotted as a dashed line when the surface spectrum of KHCC is used and as a dashed line with + symbols when the surface spectrum of EKCV97 is used. Solid lines are the corresponding curves for the full electromagnetic model (without symbol when the KHCC spectrum is used, with + symbols when the surface spectrum of EKCV97 is used).
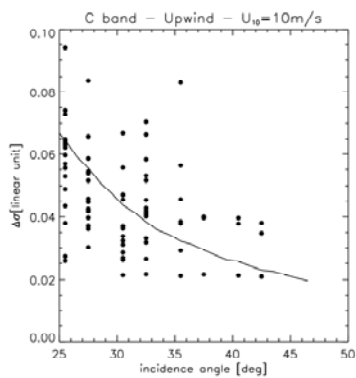
Figure 8: Difference of the NRCS in VV and HH (VV-HH in linear units) as a function of incidence angle for a wind speed of 10 m s^{-1}, and in the upwind direction. The STORM observations in C-Band are plotted as black dots. The TS model using the spectrum of KHCC is plotted as a solid line.
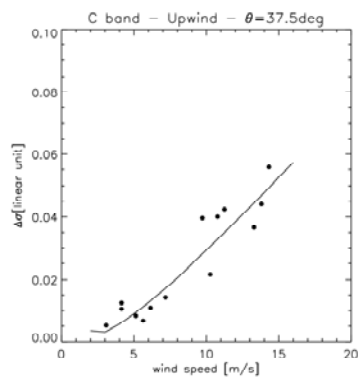
Figure 9: Same as Figure 8, but as a function of wind speed, for the incidence angle of 37.5°.
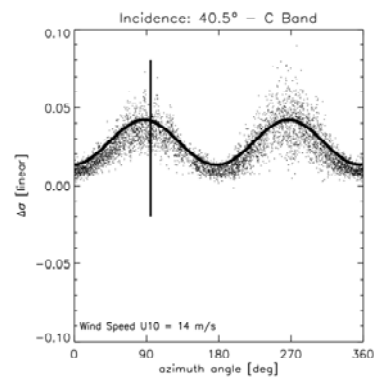
Figure 10: Same as Figure 8, but as a function of azimuth angle for the incidence angle of 40.5° and a case of strong wind (14 m s^{-1}). The vertical bar indicates the downwind direction. The TS model using the spectrum of KHCC is plotted as a solid line.
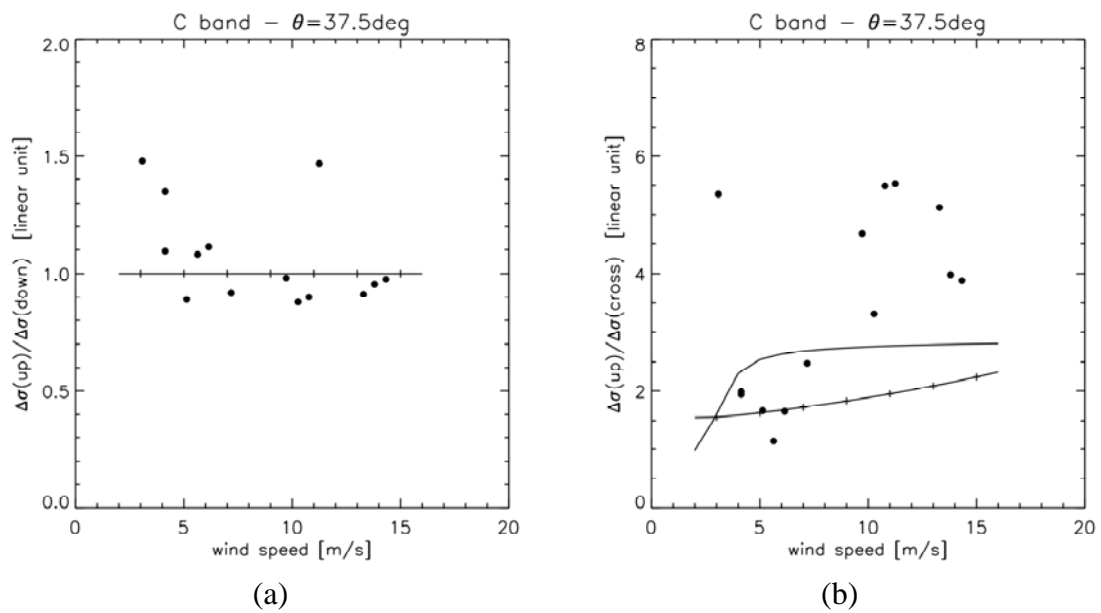
Figure 11: Upwind-to downwind ratio (a) and upwind to crosswind ratio (b) of the difference of NRCS (VV - HH in linear units) as a function of wind speed of 10 m s^{-1}, for the incidence angle of 37.5°. The STORM observations in C-Band are plotted as black dots. The TS model using the spectrum of KHCC (respectively EKCV97) is plotted as a solid (respectively solid with + symbols) line.

(a)

(b)
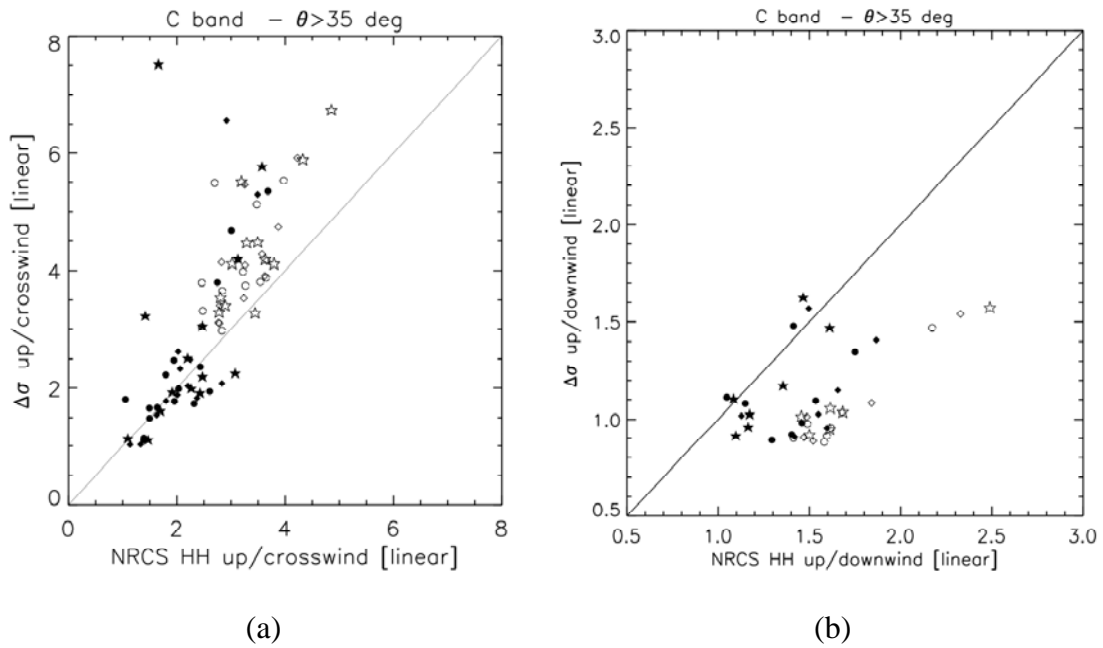
Figure 12: (a) Upwind to crosswind ratio of the NRCS difference (VV-HH) as a function of the upwind to crosswind ratio of the NRCS in HH, for all STORM data points at incidence angles of 37.5° (circles), 40.5° (diamonds), and 42.5° (stars). Closed (respectively open) symbols correspond to wind speed smaller (respectively larger) than 10 m s^{-1}. (b) same as (a) but for the Upwind to downwind ratio of the NRCS difference (VV-HH) as a function of the upwind to downwind ratio of the NRCS in HH. Note that the number of data points in Fig.12a is about twice that in Fig12 b, because observations in two cross-wind directions (left and right of upwind) have been used.
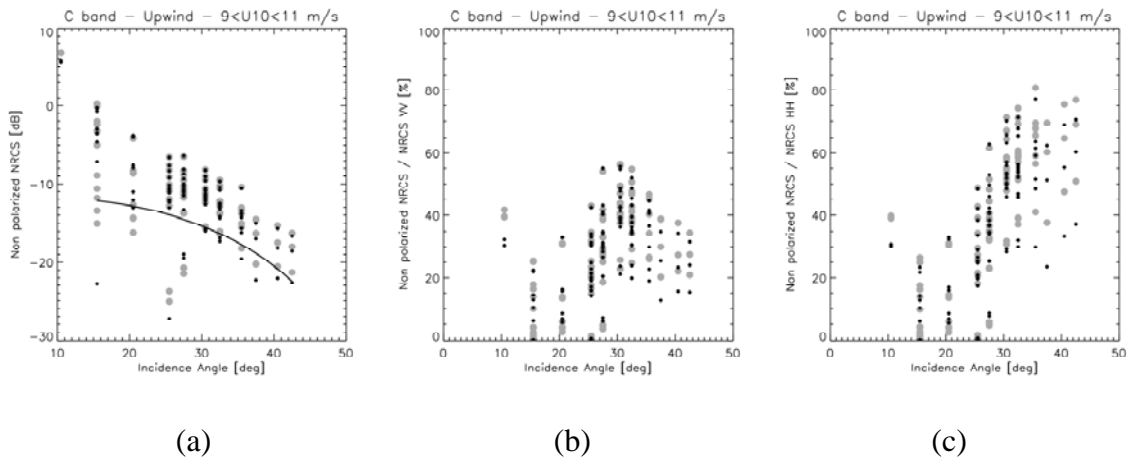
Figure 13: (a) Non-polarized part of the NRCS as a function of incidence angle for a wind speed of 10 m s^{-1} in the upwind direction. Large grey circles (respectively black small dots) are for the STORM data when the Bragg part is estimated with the KHCC spectrum (respectively with the EKCV97 spectrum). The solid line is form the present model (breaking part only). (b) Same as (a) but for the relative con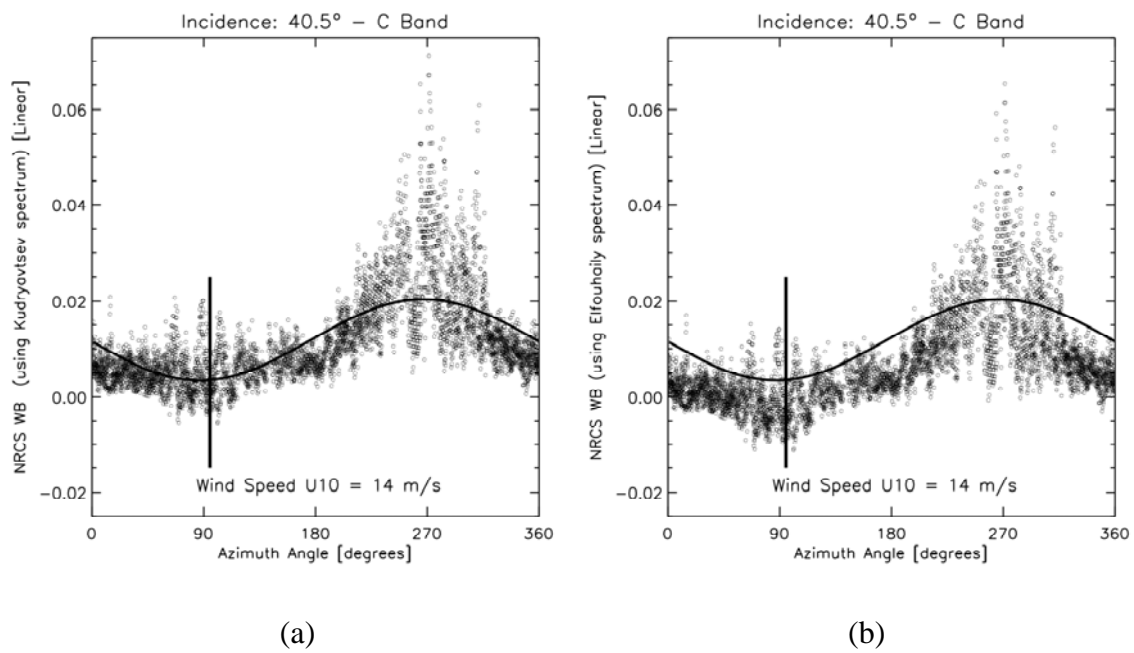tribution with respect to the total NRCS in HH polarization. (c) Same as (a) but for the relative contribution with respect to the total NRCS in VV polarization.
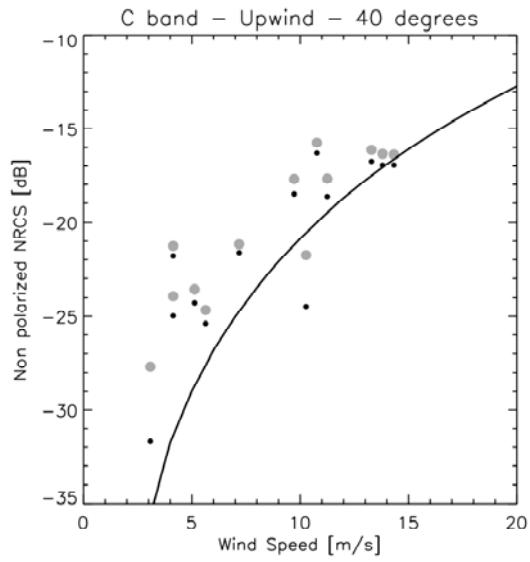
Figure 14: Same as figure 13a, but for the non-polarized part of the NRCS as a function of wind speed for and incidence angle of 37.5 °.
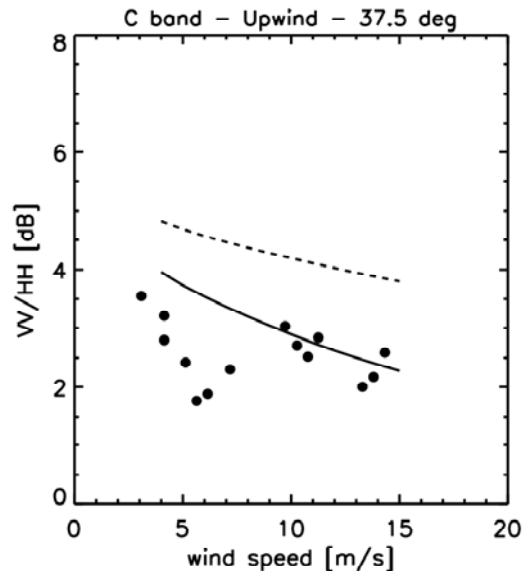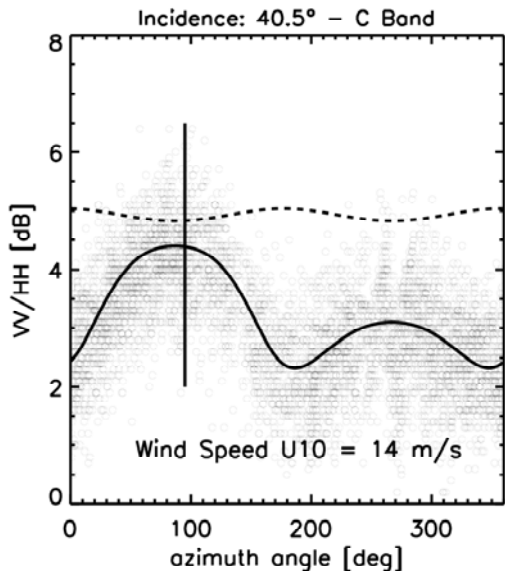
Figure 15: Non-polarized part of the NRCS as a function of azimuth angle, for the incidence angle of 40.5°, estimated from the STORM data when the Bragg part is estimated with the KHCC spectrum (Fig. 15a) and from the EKCV97 spectrum (Fig.15b). The solid line is from the present model (breaking part only). The vertical bar indicates the downwind direction.
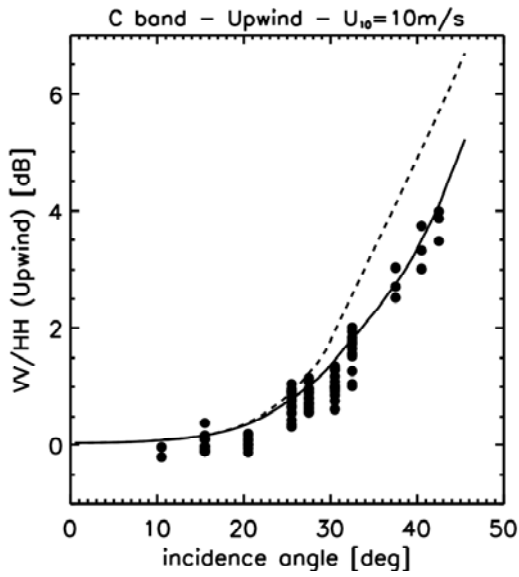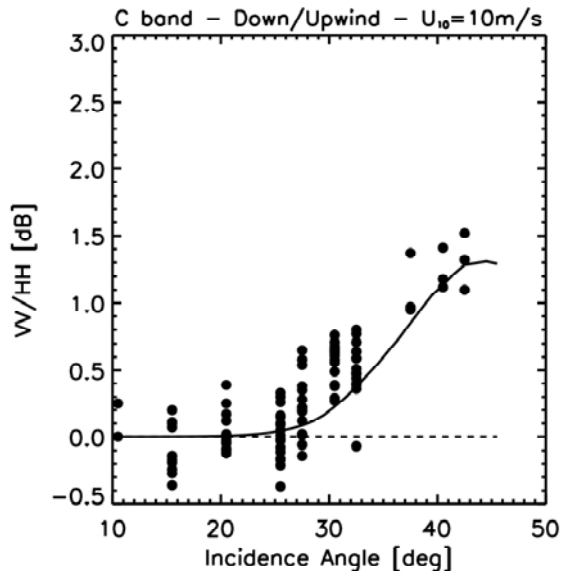
(a)

(b)

(c)

(d)

Figure 16: Results for the polarization ratio (VV/HH) plotted in dB. (a) as a function of incidence angle for a wind speed of 10 m s^{-1}, in the upwind direction . (b) as a function of wind speed for the 37.5° incidence angle. (c) as a function of azimuth angle for the same case as in Fig.3, and the incidence angle of 40.5°. The vertical bar indicates the downwind direction. (d) Upwind to downwind ratio (in dB) of the polarization ratio (HH/VV), as a function of incidence angle. In Fig.16a to 16d, the dashed line is for the TS+GO model, the solid line for the full model including the effect of breaking waves.
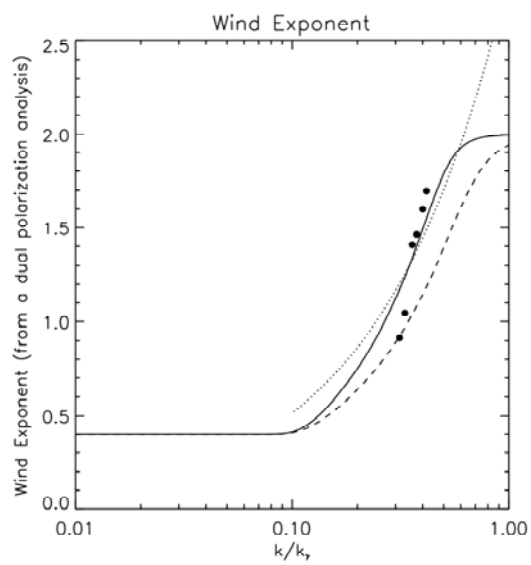
Figure A1: Radar wind exponent 2/n as a function of *k/k*
fitted from the STORM data (difference of NRCS VV-HH)
in black circle. Solid line is obtained with $k_l = 2$ and $k_h = 10$.
Dashed line $k_l = 1.5$ and $k_h = 10$. Dotted line is deduced from
the work of *Trokhimovski and Irisov* [2000].